

# Hydrogen Dynamics in Superprotonic CsHSO<sub>4</sub>

Brandon C. Wood and Nicola Marzari

*Department of Materials Science and Engineering,  
Massachusetts Institute of Technology, Cambridge, MA 02139*

We present a detailed study of proton dynamics in the hydrogen-bonded superprotonic conductor CsHSO<sub>4</sub> from first-principles molecular dynamics simulations, isolating the subtle interplay between the dynamics of the O–H chemical bonds, the O···H hydrogen bonds, and the SO<sub>4</sub> tetrahedra in promoting proton diffusion. We find that the Grotthuss mechanism of proton transport is primarily responsible for the dynamics of the chemical bonds, whereas the reorganization of the hydrogen-bond network is dominated by rapid angular hops in concert with small reorientations of the SO<sub>4</sub> tetrahedra. Frequent proton jumping across the O–H···O complex is countered by a high rate of jump reversal, which we show is connected to the dynamics of the SO<sub>4</sub> tetrahedra, resulting in a diminished CsHSO<sub>4</sub>/CsDSO<sub>4</sub> isotope effect. We also find evidence of multiple timescales for SO<sub>4</sub> reorientation events, leading to distinct diffusion mechanisms along the different crystal lattice directions. Finally, we employ graph-theoretic techniques to characterize the topology of the hydrogen-bond network and demonstrate a clear relationship between certain connectivity configurations and the likelihood for diffusive jump events.

PACS numbers: 71.15.Pd,66.30.-h,66.30.Dn,82.47.Pm

## I. INTRODUCTION AND MOTIVATION

Despite extensive efforts to realize the hydrogen economy, key technological hurdles to the widespread adoption of fuel-cell technology remain. One of the several challenges is the discovery and optimization of proton-conducting electrolyte materials for mid- to high-temperature use. Recently, a great deal of research effort has focused on anhydrous solid-state materials, in part because these offer greater flexibility in their range of operating temperatures than materials containing liquid water. Among the promising candidates are various derivatives of CsHSO<sub>4</sub>, which has been shown to exhibit high ionic conductivity ( $> 10^{-2} (\Omega\cdot\text{cm})^{-1}$ )<sup>1</sup> at target operating temperatures. Fuel-cell operation using electrolytes based upon CsHSO<sub>4</sub> and similar materials has already been successfully demonstrated in the laboratory.<sup>2,3</sup> A complete theoretical picture of the detailed atomistic mechanisms involved in proton transport in these materials is highly desirable, since such knowledge would be useful in directing future research efforts in the optimization and adaptation of new materials. Previous molecular dynamics studies<sup>4,5,6</sup> of CsHSO<sub>4</sub> based on fitted interatomic potentials have aided in highlighting the basic phenomenology of proton transport, but such investigations are unable to capture the full complexity of hydrogen bonding and electronic interactions, particularly in a dynamic environment that features rapid bond breaking and forming. The work of Ke and Tanaka<sup>7,8</sup> incorporated first-principles methodologies, but their analysis was grounded in static rather than dynamics calculations. The present study aims to elucidate the detailed atomistic pathways and mechanisms involved in hydrogen diffusion in superprotonic CsHSO<sub>4</sub> using first-principles molecular dynamics.

CsHSO<sub>4</sub> was the first known crystalline material to exhibit both hydrogen bonding and superprotonic be-

havior and has among the higher ionic conductivities of the known solid-acid materials. The room-temperature phase is monoclinic and features a static, well-defined network of hydrogen bonds. The higher-temperature superprotonic phase (usually designated Phase I) possesses a body-centered tetragonal structure and is stable above 414K.<sup>1</sup> The unit cell of this phase is depicted in Fig. 1 and consists of a lattice of SO<sub>4</sub> tetrahedra, each bonded to a hydrogen via an O–H chemical bond. Each chemically bonded hydrogen also forms an O···H hydrogen bond with an oxygen of a neighboring SO<sub>4</sub> tetrahedron. The resulting hydrogen-bond network becomes dynamic above the transition temperature and can visit a number of distinct topologies, owing to four possible oxygen binding sites for each SO<sub>4</sub> node in the network. The reigning view in the literature<sup>9,10,11,12,13</sup> is that long-range proton transport in superprotonic CsHSO<sub>4</sub> occurs as the net result of two separate mechanisms: first, the reorientation of the hydrogen-bond network by rapid rotations of the sulfate tetrahedra; and second, the hopping of the proton between oxygens of neighboring tetrahedra across the O–H···O complex. The second step has generally been considered rate limiting and is thought to occur at frequencies of the order  $10^{-9} \text{ s}^{-1}$ , whereas the first is expected to happen more frequently by at least two orders of magnitude.<sup>14,15</sup> This two-step process is often referred to collectively as the *Grotthuss mechanism*.

## II. METHOD

We performed Car-Parrinello molecular dynamics simulations<sup>16</sup> of Phase-I CsHSO<sub>4</sub> in the canonical *NVT* ensemble at temperatures of 550 K, 620 K, and 750 K (superheated), with temperatures maintained by means of a Nosé-Hoover thermostat<sup>17,18,19</sup>. Each simulation covered 25 ps of thermalized dynamics following 5 ps of

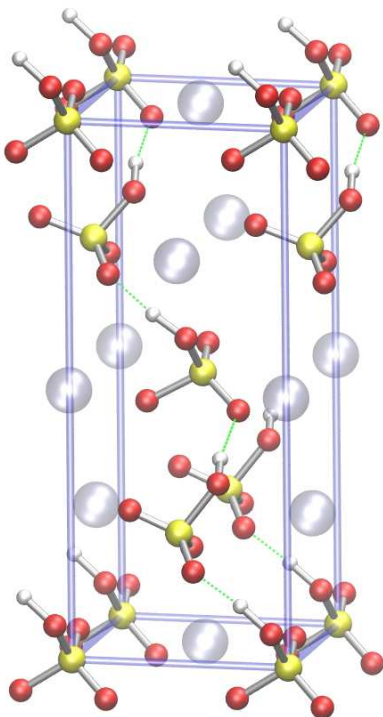


FIG. 1: (Color online) Structure of the conventional unit cell of Phase-I  $\text{CsHSO}_4$ . Hydrogen atoms are shown in white, oxygen in red, sulfur in yellow, and cesium in blue. Hydrogen bonds are denoted by broken green lines.

equilibration. This length of time proved sufficient for sampling several hundred to a thousand jump events, making statistical inferences possible. In each case, our supercell was comprised of 112 atoms (sixteen complete  $\text{CsHSO}_4$  units). Simulations were performed in a plane-wave basis using standard-valence ultrasoft pseudopotentials for hydrogen, oxygen, and sulfur; a  $6s^{0.5}5d^{0.05}6p^{0.05}$  norm-conserving pseudopotential with nonlinear core correction for cesium; and the Perdew-Burke-Ernzerhof exchange-correlation functional<sup>20</sup>. All pseudopotentials are obtainable from the Quantum-ESPRESSO website<sup>21</sup>. Cutoffs of 25 Ry and 150 Ry were used for the wavefunctions and charge density, respectively. The fictitious Car-Parrinello mass was  $\mu = 700$  with  $\Delta t = 7.5$  au, and the lattice parameter was chosen based on the experimental value just above the superionic transition temperature, taken from Ref. 22.

In presenting the results of our simulations, we have divided the dynamics into categories of chemical-bond dynamics and hydrogen-bond dynamics. We include in our definition of chemical-bond dynamics any breaking or forming of O–H chemical bonds by Grotthuss-type hopping of a proton between oxygens of neighboring tetrahedra. Any change in the hydrogen-bond network structure resulting from breaking or forming O $\cdots$ H hydrogen bonds that does *not* also involve breaking or forming O–H chemical bonds is considered in the category of

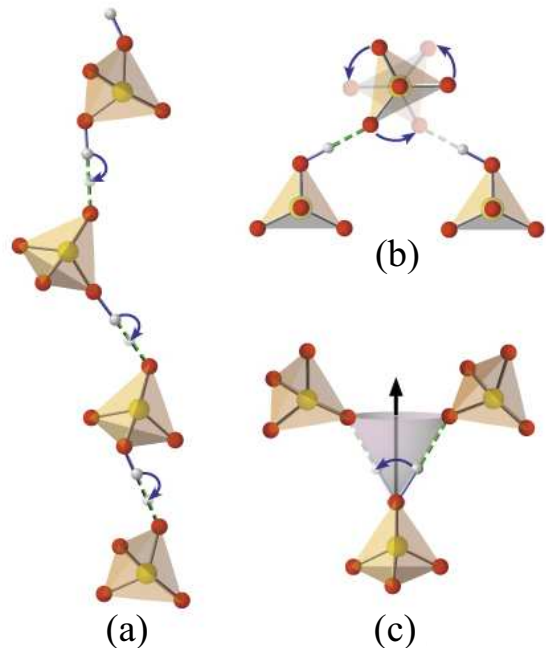


FIG. 2: (Color online) Schematic depiction of (a) a sequence of chemical-bond jumps nucleated by the formation of an  $\text{H}_2\text{SO}_4$  defect in the uppermost tetrahedron; (b) a hydrogen-bond network change induced by rotation of a host  $\text{SO}_4$  tetrahedron; and (c) a hydrogen-bond network change resulting from a direct hydrogen-bond hop with little or no rotation of the host  $\text{SO}_4$  tetrahedron. The color scheme follows that of Fig. 1, with final configurations in jumping events shown as semi-transparent.

hydrogen-bond dynamics. For additional clarity, Fig. 2 offers schematic representations of sample jump events from each category of dynamics.

### III. CHEMICAL-BOND DYNAMICS

An O–H chemical bond was defined by considering interactions with oxygens within a cutoff distance of  $R_{\text{OH}} < 1.15$  Å, which represents the initial separation between the first and second coordination peaks of the calculated oxygen-hydrogen radial pair distribution function (RDF), displayed in Fig. 3. Classification as chemical or hydrogen bond proved more difficult for O–H pairs separated by an intermediate distance  $1.15 \leq R_{\text{OH}} < 1.35$  Å due to an inherent difficulty in resolving the overlap in the first two RDF peaks in that range. The ambiguity is also noticeable upon examination of the coordination number  $n(r)$ , which is nearly flat in this region. For such O–H pairs, we instead employed a history-dependent definition, basing the bond category on the last visited unambiguous bonding regime. Under this definition, an existent O–H chemical bond was considered broken only when  $R_{\text{OH}} \geq 1.35$  Å; analogously, an exist-

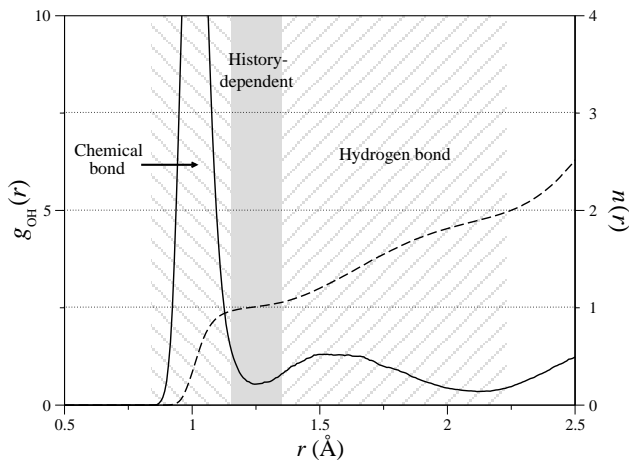


FIG. 3: The oxygen-hydrogen radial pair distribution function  $g_{\text{OH}}(r)$  (solid line, left axis) and the coordination number  $n(r)$  (dashed line, right axis), calculated from a simulation at 620 K. Regions classified as chemical and hydrogen bonds are delineated, as well as the intermediate region for which the history-dependent definition was employed.

tent  $\text{O}\cdots\text{H}$  hydrogen bond was considered broken only when  $R_{\text{OH}} < 1.15$  Å.

Within the Grotthuss mechanism, local proton transfer via a series of correlated jumps prompts changes in the chemical-bond structure. Such jumps are first nucleated by the formation of a metastable  $\text{H}_2\text{SO}_4$  defect, which subsequently propagates along the network backbone, acting as a successive proton donor for neighboring tetrahedra at each stage. The individual jumps are themselves short hops across a double-well potential barrier, where the two stable minima represent the  $\text{O}\cdots\text{H}$  and  $\text{O}-\text{H}$  distances and are separated by about 0.5 Å. A single Grotthuss hop therefore has the effect of swapping a chemical and a hydrogen bond, an action that is repeated as the proton transfer propagates across the hydrogen-bond network chain. This model of local proton transfer in superprotonic  $\text{CsHSO}_4$ , represented schematically in Fig. 2(a), is easily observable in our simulations. Indeed, just over half (51%) of the chemical-bond jumps that we register at 620 K occur as a direct result of  $\text{H}_2\text{SO}_4$  defect formation by the donation of a second proton from a neighboring tetrahedron, in accordance with the Grotthuss model. The remaining jumps are nucleated as a result of random local fluctuations in the bond structure.

It is a straightforward process to track bond formation and annihilation, and we can define a time autocorrelation function for bond existence as  $C_e(t) = \langle \alpha(0)\alpha(t) \rangle$ , where  $\alpha(t)$  is 1 if a particular type of bond exists between a given hydrogen-oxygen pair at time  $t$ , and 0 otherwise. In practice, we can improve our statistical sampling by averaging  $C_e(t)$  over all available time intervals of length  $t$  in the simulation. Using this quantity, we can obtain a detailed picture of the timescales of the chemical- and hydrogen-bond dynamics. The hydrogen-bond and chemical-bond existence autocorrelation func-

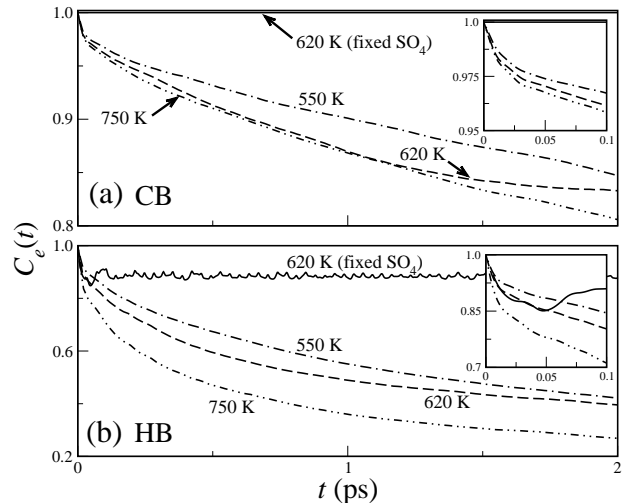


FIG. 4: Autocorrelation functions for existence of (a) chemical and (b) hydrogen bonds after a time  $t$  for simulations at 550 K, 620 K, and 750 K, as well as at 620 K with fixed sulfate tetrahedra.

tions are displayed in Fig. 4.

Beyond about 20 fs, we observe a slow exponential decay in the chemical-bond existence autocorrelation  $C_e(t)$ , with characteristic  $1/e$  decay times in the 11–15 ps range. These values are recorded in Table I, along with average overall statistical frequencies of chemical-bond jumps for each temperature and the fraction of such jumps that subsequently reverse themselves. Here a chemical-bond jump is defined as a complete exchange of a chemical and a hydrogen bond across an  $\text{O}-\text{H}\cdots\text{O}$  complex. The surprising commonality of chemical-bond jump events is reconcilable with the slow decay rate only when one considers the extremely high rate of jump reversal, which averages around 85% and features no significant variability with temperature. The combination of frequent jumping and a high, temperature-independent reversal rate is suggestive of a potential energy surface featuring an especially shallow activation barrier.

At very short times ( $< 10$  fs), we observe a fast fall-off before transitioning to the slower decay regime. In this region, we are below the timescale of any jump reversal subsequent to chemical-bond breaking and forming, resulting in a much more rapid decay. The absence of any noticeable high-frequency periodicity in Fig. 4(a) indicates that jump reversal carries no preferred timescale. Rather, it is likely that the reversal probability is a consequence of stabilization or destabilization of the local potential energy surface from  $\text{SO}_4$  tetrahedral reorientations.

As an indicator of the potential effect of the motion of the  $\text{SO}_4$  tetrahedra on the chemical- and hydrogen-bond dynamics, we have also chosen to run a second simulation at 620 K in which all ions except for the hydrogens were immobilized (denoted “fixed- $\text{SO}_4$ ” in Fig. 4). The configuration was chosen from a well-equilibrated timestep of

TABLE I: Various quantities derived from a statistical analysis of the chemical-bond dynamics at 550 K, 620 K, and 750 K. Featured columns indicate (1) the characteristic decay time  $\tau$  in an exponential fit  $Ae^{-(t/\tau)}$  of the long-time data in Fig. 4(a); (2) the average overall observed frequency  $\nu_c$  of chemical-bond jump events per ion; and (3) the fraction of these events that subsequently reverse themselves.

Temperature (K)	$\tau$ (ps)	$\nu_c$ (THz)	% rev.
550	15.2	0.58	83
620	12.5	0.80	85
750	11.2	0.94	85

the fully mobile simulation. Interestingly, all chemical-bond dynamics ceased in this simulation. This fact is particularly notable in light of previous investigations<sup>4,5,11</sup> which postulated that the most important factor in inducing chemical-bond jumping is a reduction in the O–O distance across the O–H $\cdots$ O complex due to SO<sub>4</sub> reorientation. However, in our fixed-SO<sub>4</sub> simulation, not a single chemical-bond jump event was registered, despite the continuous presence of O–O distances as short as 2.30 Å across O–H $\cdots$ O complexes. Notably, this value is approximately 0.15 Å shorter than the average O–O distance across O–H $\cdots$ O complexes of hydrogens actively involved in chemical-bond jumps in the fully mobile simulation. Moreover, in our fully mobile simulations, we find only a 0.01 Å difference between the average O–O distances across O–H $\cdots$ O complexes of hydrogens involved in chemical-bond jumping events and ordinary hydrogens not involved in jump events of any sort. We therefore conclude that the primary contribution of the SO<sub>4</sub> tetrahedra to chemical-bond jumping results from their vibrational or rotational dynamics rather than simply their instantaneous orientation. Also, despite the low barrier for Grothaus-style chemical-bond hopping, dynamic degrees of freedom connected solely to the hydrogens are nevertheless insufficient to permit chemical-bond breaking or forming, detailing the necessary role of the oxygen modes in that process.

Our results reveal that the general chemical-bond jump frequency is relatively high; moreover, it is of the same order as the hydrogen-bond dynamics (compare Tables I and II). This contrasts with the view of chemical-bond jumping as substantially rate limiting and differing in timescale from the hydrogen-bond dynamics by two or more orders of magnitude. We instead find that the limiting factor in the *effective* rate of chemical-bond jumps is the extraordinarily high rate of jump reversal, which we suggest is linked to the dynamics of the SO<sub>4</sub> tetrahedra. Yet even when jump reversals are considered, our effective chemical-bond dynamics are significantly faster than the proposed nanosecond scale. Instead, our results are consistent with recent experiments<sup>23,24</sup> pointing to much faster chemical-bond dynamics than have hitherto been assumed, perhaps even on the picosecond scale.

It should be noted that in our analysis of jump re-

versals, we have considered only *single* jumps that are subsequently reversed. In so doing, we have neglected the reversal of collective sequences of jump events. Such higher-order jump sequences are especially difficult to properly consider given the inherent time- and length-scale limitations imposed by the first-principles methodology. It is expected that accounting for the potential reversal of such longer sequences would limit the number of counted “successful” jumps (those contributing to macroscopic proton diffusion). The magnitude of any such limitation is difficult to predict, however.

#### IV. HYDROGEN-BOND DYNAMICS

For the purposes of this work, we have defined a hydrogen bond in terms of the oxygen-hydrogen distance alone, with the additional restriction that hydrogen bonding cannot involve oxygens attached to the same host sulfate tetrahedron as the hydrogen. Under this definition, the usual practice of restricting  $\angle\text{O–H}\cdots\text{O}$  had no appreciable effect on the counted hydrogen bonds and was omitted for sake of simplicity. A hydrogen-bond maximum cutoff distance of  $R_{\text{OH}} < 2.23$  Å was chosen based on the distance for which the coordination number  $n(r) = 2$ , indicating the tail end of the second coordination peak (associated with H $\cdots$ O) in the calculated oxygen-hydrogen RDF (Fig. 3). The minimum cutoff of  $R_{\text{OH}} \geq 1.35$  Å was chosen based on the clear point of separation for the second RDF peak and the end of the plateau region in the coordination number. As for the chemical bonds, we implement a history-dependent definition for categorizing bonds in the intermediate range of  $1.15 \leq R_{\text{OH}} < 1.35$  Å.

Fig. 4(b) shows the bond-existence autocorrelation function  $C_e(t)$  for the hydrogen bonds in simulations at 550 K, 620 K, 750 K, and for the “fixed-SO<sub>4</sub>” simulation at 620 K in which all ions except the hydrogens are immobilized. At longer times, we observe an exponential decay of the hydrogen bonds for the fully mobile simulations that far outpaces that of the chemical bonds. The graph also reveals that at short times ( $< 50$  fs; see figure inset), the hydrogen bond network in the fixed-SO<sub>4</sub> simulation remains very dynamic, approximately following the equivalent curve for the fully mobile system. However,  $C_e(t)$  soon begins to oscillate around a fixed running average, indicating repeated visitation of a few alternating configurations. Interestingly, the overall frequency of hydrogen-bond breaking is actually greater for the fixed-SO<sub>4</sub> simulation than for the fully mobile simulation.

Table II contains these hydrogen-bond breaking frequencies, as well as likelihoods for reversal of hydrogen-bond network reorganization events. In addition to providing overall values, we have divided the hydrogen-bond dynamics into two categories based on the location of the newly formed hydrogen bond with respect to its predecessor. Our first category consists of hydrogen bonds transferred between oxygens of the same destination SO<sub>4</sub> tetrahedron; the second contains hydrogen bonds trans-

ferred between oxygens of neighboring  $\text{SO}_4$  tetrahedra. In practice, higher temperatures generally show a greater preference for exchanges between oxygens of different tetrahedra than do lower temperatures, but in all cases, such exchanges outnumber those between oxygens of the same tetrahedron by a margin of two or three to one. Fixing the  $\text{SO}_4$  tetrahedra pushes that margin even further.

Unlike in the case of the chemical-bond dynamics, freezing the degrees of freedom of the  $\text{SO}_4$  tetrahedra does not prevent reconfiguration of the hydrogen-bond network via bond breaking and forming. In fact, Table II reveals that inhibiting  $\text{SO}_4$  rotation actually enhances the frequency of hydrogen-bond breaking and forming, particularly for bonds exchanged between oxygens of neighboring tetrahedra. However, some degree of rotation is required in order to visit a larger region of configuration space and prevent repeated visitation of identical configurations, a vital stipulation for macroscopic proton transport.

The point of separation of the hydrogen-bond autocorrelation curves for the fixed- $\text{SO}_4$  and fully mobile system, as seen in the inset of Fig. 4(b), can be interpreted physically as a characteristic reversal time: if a newly formed hydrogen bond is to be accepted, enough  $\text{SO}_4$  rotation must occur within the approximately 50 fs window to sufficiently alter and imbalance the energy landscape, thereby minimizing likelihood of back hopping. Accordingly, Table II shows that the observed fraction of hydrogen-bond network reorganization events that subsequently reverse themselves within this time period in the fixed- $\text{SO}_4$  simulation is more than double that of the fully mobile simulation at the same temperature (38% versus 77%).

A Fourier transform of the hydrogen-bond existence autocorrelation function  $C_e(t)$  gives a good measure of the typical oscillation frequencies for the hydrogen-bond forming and breaking in the fixed- $\text{SO}_4$  simulation. Fig. 5 compares this result to the vibrational density of states for the hydrogens in that simulation as well as in the fully mobile simulation. A comparison of Figs. 5(b) and (c) allows us to distinguish the hydrogen vibrational modes that are not directly connected to hydrogen-bond breaking from those that are. Those not linked to changes in the hydrogen-bond network are represented by clusters of broader peaks around 15–20 THz, 30–40 THz, and 80–95 THz. Of these, the two lowest-frequency clusters most likely represent bending modes, whereas the highest-frequency cluster contains stretching modes. The primary peaks associated with bond breaking and forming are a low-frequency peak near 9 THz and a fundamental second peak at 28 THz, along with its accompanying overtone peaks at higher frequencies. Since these peaks are completely suppressed in the result for the fully mobile simulation shown in Fig. 5(a), they represent the signature oscillations inhibited upon stabilization of new configurations by reorientations of the  $\text{SO}_4$  tetrahedra. Notably, the half-period switching time represented by

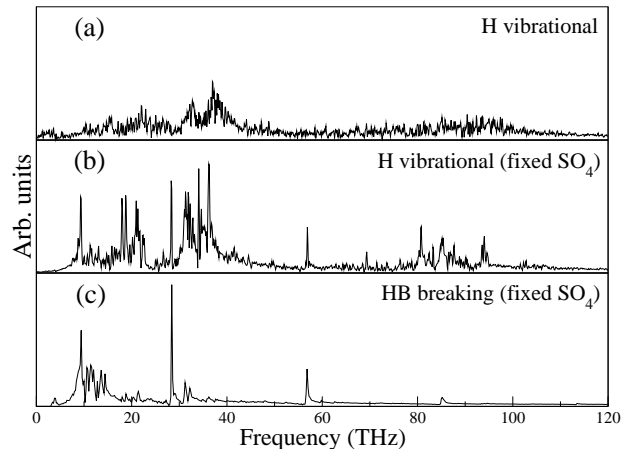


FIG. 5: Vibrational density of states for the protons in (a) the fully mobile and (b) the fixed- $\text{SO}_4$  simulations, along with (c) the hydrogen-bond switching frequency spectrum for the fixed- $\text{SO}_4$  simulation. Data are from simulations at 620 K, and densities of states were obtained from a Fourier transform of the appropriate velocity autocorrelation function.

the low-frequency peak matches the characteristic reversal threshold obtained from Fig. 4. The higher-frequency peak at 28 THz is also evident in that same figure, appearing as shallow oscillations at short timescales. The existence of pronounced overtones for the 28 THz peak in both the vibrational and bond-breaking frequency spectra suggests significant anharmonicity in the potential for the  $\text{H}\cdots\text{O}$  bond.

Since the primary effect of suppressing  $\text{SO}_4$  rotation is to encourage reversal of hydrogen-bond network reorientation phenomena rather than to inhibit such reorientations altogether,  $\text{SO}_4$  rotation alone cannot satisfactorily account for the full network dynamics. Rather, we observe that the dominant mechanism for hydrogen-bond network reorganization involves hydrogen-bond transitions that are best described as rapid, discrete angular jumps between two stable states rather than as a smooth evolution driven by  $\text{SO}_4$  tetrahedral rotations, as has generally been proposed previously. These two states correspond to different orientations for which the  $\angle\text{S-O-H}$  angle for chemically bonded hydrogens is maintained near the tetrahedral angle of  $109.5^\circ$ . This phenomenon is depicted schematically in Fig. 2(c) and resembles the proposed diffusion mechanism in a recent simulation of liquid water<sup>25</sup>.

Additional evidence for the angular hopping model appears in Fig. 6, which outlines distributions for certain geometrically relevant angles in both the fully mobile and fixed- $\text{SO}_4$  simulations at 620 K. The  $\angle\text{S-O-H}$  angles for chemically bonded protons have a relatively small spread and are peaked around the described tetrahedral geometry. Angles greater than  $145^\circ$  are not represented, indicating that the protons lie primarily on the surface of a cone centered on the S–O bond and with a half-angle

TABLE II: Various quantities derived from a statistical analysis of the hydrogen-bond dynamics at 550 K, 620 K, 750 K, and for the fixed-SO<sub>4</sub> simulation at 620 K. The data is divided into statistics for hydrogen-bond exchanges between oxygens of the same SO<sub>4</sub> tetrahedron, those of different SO<sub>4</sub> tetrahedra, and overall totals for either type of exchange. Featured columns include (1) the fraction of total hydrogen-bond exchanges representing a particular class of exchange; (2) the average overall observed frequency  $\nu_h$  of hydrogen-bond jump events per ion; and (3) the fraction of these events that reverse themselves within a 50 fs window.

Temperature (K)	Same SO <sub>4</sub>			Different SO <sub>4</sub>			Overall	
	% tot.	$\nu_h$ (THz)	% rev.	% tot.	$\nu_h$ (THz)	% rev.	$\nu_h$ (THz)	% rev.
550	38	0.47	49	62	0.79	34	1.16	40
620	25	0.58	38	75	1.72	38	2.30	38
750	23	1.01	35	77	3.45	39	4.46	39
620 (fixed-SO <sub>4</sub> )	21	0.96	67	79	3.57	79	4.53	77

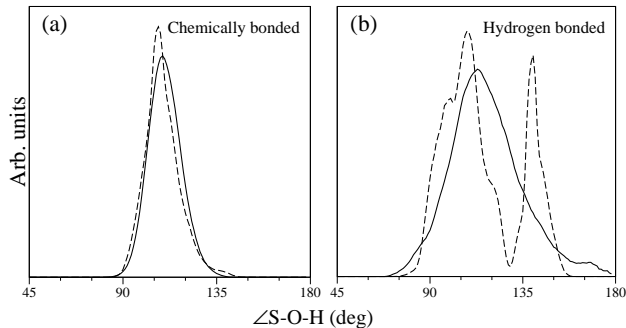


FIG. 6: S–O–H angles for (a) chemically bonded and (b) hydrogen-bonded protons in fully mobile (solid) and fixed-SO<sub>4</sub> (dashed) simulations at 620 K.

of 65–70°. Notably, the angular distribution does not change appreciably between the fully mobile and fixed-SO<sub>4</sub> simulations. Although hydrogen-bonded protons are generally less constrained, the  $\angle S-O\cdots H$  distributions for both simulations are still peaked near 110°. However, for the fixed-SO<sub>4</sub> simulation, a second peak appears in the angular distribution at around 140° as a byproduct of the hydrogen-bond hops. The separation of the two peaks for the fixed-SO<sub>4</sub> case in Fig. 6(b) indicates that generally a net SO<sub>4</sub> tetrahedral reorientation of around 30°, involving either the hydrogen-bond donor or acceptor tetrahedron, accompanies the hop to alleviate the lattice strain it induces. This value for the SO<sub>4</sub> angular rotation agrees well with what has been proposed in the literature<sup>10,22,26,27</sup>, but our resolution is insufficient to pinpoint which of the particular competing models is most likely to be correct. Such reorientation is also responsible for altering the potential energy surface to minimize back hopping.

## V. ROTATION OF SO<sub>4</sub> TETRAHEDRA

Since it has already been established that the 30° reorientation of the SO<sub>4</sub> tetrahedra must take place within a 50 fs window to maximize the potential for non-reversing

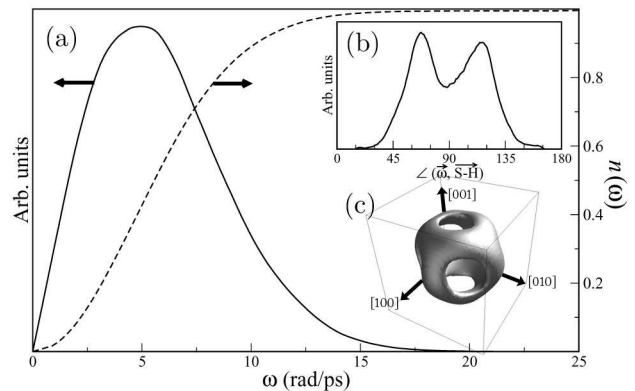


FIG. 7: (a) Angular velocity profile for the SO<sub>4</sub> tetrahedra at 620 K (solid), along with the corresponding fraction of tetrahedra  $n(\omega)$  with velocities  $\leq \omega$  (dashed). Inset (b) shows the angular distribution of the sulfate tetrahedral axes of rotation  $\hat{\omega}$  with respect to  $\hat{f}_{SH}$ , and inset (c) shows the radial distribution of the  $\hat{\omega}$  vectors in space with respect to the primary crystallographic axes.

transitions, we can obtain 10.5 rad/ps as a back-of-the-envelope estimate for the minimum SO<sub>4</sub> angular velocity required to prevent reversal following a hydrogen-bond switch. The SO<sub>4</sub> angular velocities follow a Boltzmann distribution and are plotted in Fig. 7. The plot reveals that velocities of this magnitude, although somewhat rare, are indeed accessible, representing about 8–9% of the SO<sub>4</sub> tetrahedra in the 620 K simulation at any given time.

Fig. 7(c) shows an isosurface of the angular velocity unit vectors  $\hat{\omega}$  for the rotation of the SO<sub>4</sub> tetrahedra, averaged over all such groups in the 620 K simulation. Areas of high density therefore represent preferred axes of rotation, a clear structure for which is visible in the figure. These rotation axes do not align towards the chemically bonded hydrogen or its accompanying oxygen, as is evident from Fig. 7(b). Instead, they orient along the edges of a cube rotated  $\pi/4$  in the (001) crystal plane with respect to the conventional unit cell, thereby correlating with the centers of the nearest-neighbor tetra-

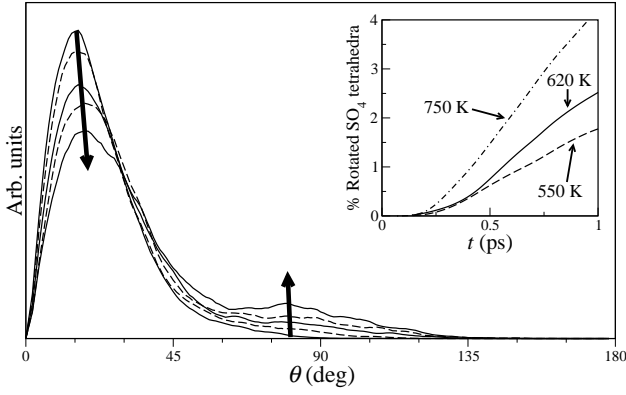


FIG. 8: Distribution of angular distances traveled by sulfate tetrahedra as a function of time at 620 K. Successive curves represent values at 0.5, 1, 2, 3, and 5 ps. The inset gives a measure of the fraction of tetrahedra with greater than  $70^\circ$  rotation from their initial positions as a function of time at 550 K, 620 K, and 750 K.

hedra. The  $\text{SO}_4$  rotational orientations thus appear to be governed by the locations of nearby  $\text{SO}_4$  tetrahedra rather than the location of the locally bonded hydrogen or the orientation of its corresponding chemical bond. In other terms, rotational axes align along  $\hat{\mathbf{r}}_{\text{SS}}$  rather than  $\hat{\mathbf{r}}_{\text{SH}}$  or  $\hat{\mathbf{r}}_{\text{SO}}$ .

In view of the fact that angular jumps alone, stabilized by small, rapid tetrahedral reorientation events of about  $30^\circ$ , account for much of the hydrogen bond network dynamics, it is desirable to analyze and requantify the relative contribution of larger-scale rotational motion. Fig. 8, which shows the averaged distributions of angular distances traveled by  $\text{SO}_4$  tetrahedra as a function of time, illustrates one effect of slower rotational dynamics. There is evidence of the appearance of a second peak in the distributions representing a new, stable equilibrium configuration at  $75\text{--}80^\circ$  rotation with respect to the original tetrahedral orientation. This peak begins to manifest in statistically measurable quantities only after 250 fs (see inset of figure), making the quickest of such reorientation events several times slower than the timescale of the fast  $30^\circ$  reorientation event described previously. We note that the faster dynamics with the smaller reorientation angle cannot be distinguished in Fig. 8 since it is buried within the first peak, which primarily depicts the fast librational modes.

Additional confirmation of the existence of multiple distinct timescales for the tetrahedral orientation can be seen in Fig. 9, which portrays the angular time autocorrelation of tetrahedral configurations. We calculate this quantity according to  $C_\theta(t) = \langle \hat{\mathbf{r}}_{\text{SO}}(t) \cdot \hat{\mathbf{r}}_{\text{SO}}(0) \rangle$ , producing a measure of the cosine of the average angular distance traveled by an S–O unit vector  $\hat{\mathbf{r}}_{\text{SO}}$  as a function of time. As before, we maximize our available statistics by averaging  $C_\theta(t)$  over all available time intervals of length  $t$  in the simulation. The slower rotation events manifest

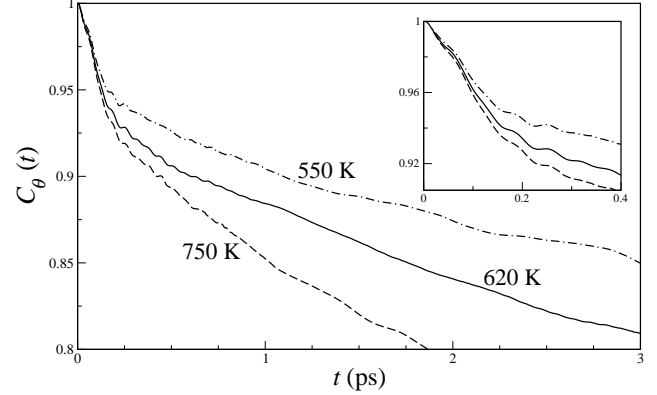


FIG. 9: Autocorrelation function for angular distance traveled between  $\text{SO}_4$  tetrahedral orientations separated by time  $t$ .

themselves as a quasi-linear decay in the autocorrelation at longer times. At short times ( $< 250$  fs), the slope is appreciably steeper, indicating faster dynamics on average. Expectedly, the separation between these two regimes agrees with the timescale of the emergence of the slow rotation in Fig. 8. In addition, a shoulder indicating the timescale of a rotation to a nearby local minima is clearly distinguishable at around 50–60 fs, in agreement with our previous indicators of fast dynamics on that scale. This shoulder repeats itself as periodic oscillations and is also detectable as a peak in the Fourier transform (not shown) of the curve in Fig. 9. The oscillations also span the intermediate region in which rotations of both short and long timescales are manifest before they are lost in the slower dynamics at longer times. We further note that changes in temperature have no appreciable effect on the timescale of the fast rotation, as measured by the locations of the shoulders and oscillations in the figure. This is consistent with a picture in which the reorientation is connected to a hydrogen-bond hop and therefore has an almost negligible rotational barrier.

The anisotropy of the diffusion tensor for  $\text{CsHSO}_4$  has been documented experimentally<sup>28</sup> and is a geometric consequence of the greater angular distance that must be traversed by a diffusing proton traveling across two sulfate layers along the  $[001]$  or  $[00\bar{1}]$  directions ( $117^\circ$ ) compared to a similar journey in a  $\{001\}$  plane ( $78^\circ$ ). Our results confirm that diffusion parallel to the  $(001)$  plane dominates: the directional mean-square displacement of the hydrogen atoms rises 2.5 to 5 times faster along the  $[010]$  or  $[100]$  directions than along the  $[001]$  direction, with higher temperatures favoring higher anisotropy. This disparity suggests a different dominant mechanism for diffusion along a  $\langle 001 \rangle$  direction, in part because the angular distance is too great to be easily accommodated by the described hydrogen bond hopping mechanism, and in part because the corresponding angular velocities that would have to be reached by the sulfate tetrahedra to prevent backhopping in such a scheme are unreasonably high. Instead, we find that slower  $\text{SO}_4$  ro-

tation plays the dominant role in overcoming the larger barrier, in line with the more traditional model of proton transport in  $\text{CsHSO}_4$  (depicted in Fig. 2(b)). In this case, the dynamics are slow enough that the timescale of the large-scale rotation is no longer a hindrance. We further note that the approximately  $40^\circ$  difference in the angular distance that must be traveled in the  $[001]$  direction with respect to a similar journey in the  $(001)$  plane, combined with the aforementioned  $30^\circ$   $\text{SO}_4$  reorientation, satisfactorily accounts for the appearance of the second peak in Fig. 8 to within a rough estimate. This suggests that for diffusion in the  $[001]$  direction, the slow rotation is probably followed by a rapid hydrogen-bond hop, although the former clearly determines the timescale.

## VI. HYDROGEN-BOND NETWORK TOPOLOGY

We have also analyzed the basic topology of the hydrogen-bond network. Table III shows the relative probabilities of various  $\text{SO}_4$  bonding configurations at 550 K, 620 K, and 750 K, organized according to the number of hydrogen bonds donated ( $N_d$ ) and accepted ( $N_a$ ) by the  $\text{SO}_4$  tetrahedron. In our definition, a donated bond is formed between a local chemically bonded hydrogen and an oxygen on a neighboring tetrahedron; an accepted bond is a hydrogen bond formed between a local oxygen and a hydrogen that is chemically bonded to a neighboring tetrahedron. For an ideal one-dimensional network, one would expect all tetrahedra to have  $N_d=N_a=1$ . In our simulations, we observe this type of ordinary link only 41–61% of the time, suggesting the actual network topology is much more complicated. Other highly probable configurations include one with  $(N_a, N_d) = (1, 0)$ , which can be thought of as a terminator in the hydrogen bond network (18–26%); and one with  $(N_a, N_d) = (1, 2)$ , which can be interpreted as a network branching point (8–14%). According to the table, there is a great deal of variability in the number of hydrogen-bond donors  $N_d$ , but configurations with  $N_a \neq 1$  are comparatively rare. The primary effect of increasing the temperature seems to be a decrease in the number of ordinary linear network links with  $N_d=N_a=1$  in favor of network terminators with  $(N_a, N_d) = (1, 0)$ , resulting in a more nodal network. Some of the rare (but nonetheless statistically significant) configurations are signatures of Grotthus-type jumps in progress: immediately following a standard chemical-bond jump from one  $\text{SO}_4$  tetrahedron to another, nucleated at a link in an ordinary linear chain, the source tetrahedron registers a topological configuration of the form  $(N_a, N_d) = (2, 0)$ , whereas the  $\text{H}_2\text{SO}_4$  destination tetrahedron acquires a configuration of the form  $(N_a, N_d) = (0, 2)$ .

Table IV lists the average lifetimes of the local topologies listed in Table III. Although these values are averages and do not account for the complete distribution of possible lifetimes as do the autocorrelation curves of

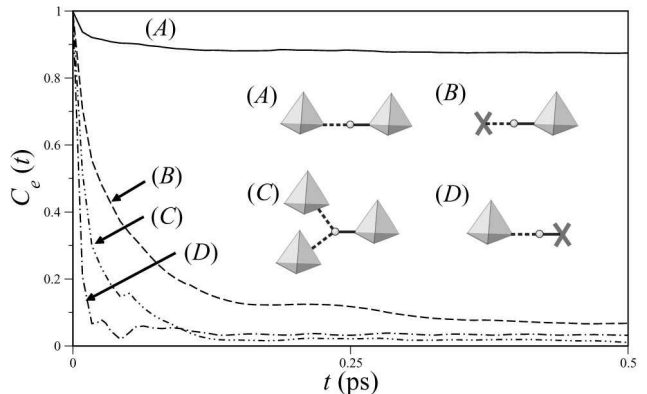


FIG. 10: Existence autocorrelation functions for four of the most likely tetrahedral bonding configurations. In the schematic diagrams, a solid line represents a chemical bond, a dashed line represents a hydrogen bond, and an “X” indicates the absence of a bond.

Fig. 10, they are nonetheless useful for purposes of qualitative comparison. Lifetimes are generally well correlated with relative frequencies, with hydrogen bonding to a single secondary tetrahedron ( $N_a=1$ ) acting as a stabilizing force. As the temperature increases, the lifetimes of configurations with  $N_a \neq 1$  are affected very little, but we observe a sharp systematic decline in nearly all configurations with  $N_a=1$ . Notably, this trend does not always follow that of the relative frequencies in Table III. For example, network terminators with  $(N_a, N_d) = (1, 0)$  exhibit a decrease in average lifetime but an increase in their overall commonality, suggesting a more nodal but also more dynamic network at high temperatures.

Tables III and IV neglect hydrogen bonds to the same  $\text{SO}_4$  tetrahedron as the host, in accordance with our original definition of the hydrogen bond. However, if we relax the hydrogen-bonding restriction requiring bonds to be between oxygens of different tetrahedra, we find that these “self-hydrogen bonded defects”, although short-lived, are nonetheless relatively common, representing about 3% of the total  $\text{O} \cdots \text{H}$  interactions at 620 K. Moreover, we find that hydrogens involved in chemical and hydrogen bonds to the same  $\text{SO}_4$  tetrahedron do not permit simultaneous hydrogen bonding to oxygens of neighboring tetrahedra, meaning these complexes function as terminators for the hydrogen-bond network chains. Also, the average velocity of oxygens in self-hydrogen bonded  $\text{SO}_4$  complexes is consistently about 10% higher on average than in ordinary complexes with  $N_d=N_a=1$ . This suggests that underbonding lessens the degree of constraint and enhances oxygen mobility in such units, likely aiding further reorganization of the hydrogen-bond network.

In addition to examining the network topology in terms of connectivity between neighboring  $\text{SO}_4$  tetrahedra, one can obtain a slightly different topological gauge by looking at the number of chemical and hydrogen bonds



TABLE III: Observed relative probabilities (%) of  $\text{SO}_4$  bonding configurations, organized according to the number of hydrogen bonds accepted (rows) and the number donated (columns) by the  $\text{SO}_4$  tetrahedron. Data are from simulations at 550/620/750 K.

$\% \text{ Prob.}$	$N_d = 0$	$N_d = 1$	$N_d = 2$	$N_d = 3$
$N_a = 0$	2 / 3 / 7	3 / 4 / 6	1 / 1 / 2	1 / 1 / 1
$N_a = 1$	18 / 22 / 26	61 / 53 / 41	11 / 15 / 14	1 / 1 / 1
$N_a = 2$	1 / 1 / 2	<1 / <1 / 1	0 / 0 / 0	0 / 0 / 0

TABLE IV: Average lifetimes (fs) of  $\text{SO}_4$  bonding configurations, organized according to the number of hydrogen bonds accepted (rows) and the number donated (columns) by the tetrahedron. Data are from simulations at 550/620/750 K.

$Lifetime \text{ (fs)}$	$N_d = 0$	$N_d = 1$	$N_d = 2$	$N_d = 3$
$N_a = 0$	48 / 53 / 55	47 / 43 / 42	21 / 19 / 25	34 / 21 / 24
$N_a = 1$	176 / 159 / 117	238 / 169 / 105	128 / 119 / 75	81 / 92 / 54
$N_a = 2$	27 / 20 / 24	20 / 17 / 20	0 / 0 / 0	0 / 0 / 0

formed by a single proton. Fig. 10 shows the existence autocorrelation curves for four of the most common topologically distinct bonding configurations for a proton. These curves give an idea of the characteristic decay times for each configuration. The result for a standard bonding configuration, in which a proton forms one chemical and one hydrogen bond ( $A$ ) is shown for timescale reference. We note that topologies with protons forming a single chemical bond but no hydrogen bond ( $B$ ) are surprisingly stable, with a characteristic decay time that is relatively large on the timescale of both the hydrogen-bond hopping and its corresponding strain-relaxing  $\text{SO}_4$  reorientation. Defects of this class are less constrained and more mobile than their ordinary counterparts, and as in the case of the self-hydrogen bonded complexes, the increased mobility facilitates network reorganization much more readily. Network-branching configurations with multiple hydrogen bonds ( $C$ ) play a more direct role in the reorganization of the hydrogen-bond network but have only intermediate stability. Configurations with no chemical bond ( $D$ ) are extremely short-lived.

Techniques involving the graph-theoretic adjacency matrix (see Appendix) also offer a convenient way of characterizing the topology of the overall network and extracting configurations most likely to induce a diffusive event. In particular, we are able to further classify the network topology in terms of *rings*, meaning some part of the network ultimately connects back to itself in a closed loop; and *chains*, meaning the network either remains linear or branches, with the restriction that any two network vertices are connected by exactly one unique directed path (i.e., a graph-theoretic tree). The specifics of our classification algorithm are described in the Appendix. It should be noted that such a dichotomy requires classification of every node as either a chain or a ring but does not allow any given node to be doubly counted as belonging to both categories. Table V lists the likelihood of finding a tetrahedron in various ring and chain topologies in an ordinary simulation timestep versus a timestep immediately preceding a chemical-

hydrogen-bond jump event.

For ordinary configurations not involving a jump event, the network favors rings over chains at 550 K, whereas the trend is reversed at 750 K. The intermediate temperature of 620 K is a topological transition zone and shows a marked increase in configurations simultaneously containing both rings and chains. There is also a notable decrease in the average length of a chain and a slight decrease in the average size of a ring at 620 K compared to the other temperatures. This is a further indication that the network is midway in a transition process from primarily rings to primarily chains, as a network configuration containing both would tend to inhibit the growth of either one at the expense of the other.

Our findings indicate that at all temperatures, the presence of topological chains has a dramatic effect in enhancing the likelihood of occurrence of either sort of jump event. Conversely, the presence of rings strongly inhibits jumping. The trend is much more pronounced when one examines frames containing either rings or chains as the only topological species: in frames preceding a chemical-bond jump, we see a 23–24% increase in likelihood of the frame to contain exclusively chains and a corresponding 13–23% decrease in its likelihood to contain exclusively rings, as compared to a frame in an ordinary non-jumping configuration. This difference is especially pronounced at higher temperatures. Nonuniform configurations containing both rings and chains also show an overall decrease in jump likelihood. The trends in the chain and ring data also evidence that from a purely topological perspective, a configuration favorable for a hydrogen-bond jump lies midway between an ordinary configuration and one favorable for a chemical-bond jump. We conclude that the network ring and chain topology is a good indicator of both hydrogen- and chemical-bond jump likelihood and is substantially more effective in that capacity than the measure of the oxygen-oxygen distance across the  $\text{O-H}\cdots\text{O}$  complex.

It is worthwhile mentioning that periodic boundary conditions and limited supercell sizes have two major

topological consequences that must be considered in any analysis: first, they decrease the maximum length of chains that can be formed; and second, they tend to artificially inflate the number of smaller rings, since creation of periodic images tends to wrap the network back onto itself prematurely. As such, the values in Table V should not be taken as absolutes, but qualitative comparisons are nonetheless useful and relevant.

## VII. PROTON KINETICS AND THE ISOTOPE EFFECT

We can estimate the general three-dimensional proton self-diffusion coefficient from the mean-square displacement (MSD) using the Einstein relation:  $D_H = \lim_{t \rightarrow \infty} \frac{1}{6t} \langle \text{MSD}(t) \rangle$ . Using this method, we estimate  $D_H$  in our simulations to be  $1.8\text{--}3.5 \times 10^{-6}$  cm<sup>2</sup>/s over the 550–750 K temperature range, about an order of magnitude greater than extrapolations of experimental measurements to the same range ( $1.9\text{--}3.4 \times 10^{-7}$  cm<sup>2</sup>/s)<sup>15</sup>. However, despite the error in the magnitude of the calculated diffusion coefficients, we nonetheless observe the proper scaling of  $D_H$  with temperature, indicating correct calculation of the energetic barriers for diffusion.

Multiple factors may contribute to the discrepancy of the calculated diffusion coefficients with experiment. First, calculations of these coefficients are notoriously difficult to converge, particularly when diffusivities are small and statistics are limited. One possible gauge of accuracy in the calculation can be achieved by comparing the result to the same quantity found using the Green-Kubo relation. The Green-Kubo method is based on the velocity autocorrelation function rather than the mean-square displacement; however, this method generally exhibits even poorer convergence in the absence of excellent statistics. Instead, we estimate the accuracy of our diffusion coefficients based on twice the standard error in the determination of the mean-square displacement slope, which results in an error estimate of  $\pm 15\%$ .

Second, we have already mentioned the difficulty in accounting for correlation and reversal of collective sequences of jump events. In the limit of the short length- and timescales accessible by first-principles methods, it is expected that any diffusive correlations that persist over large regions of either time or space would be lost, resulting in inflated diffusion statistics. Similarly, jump events that remain localized due to high incidences of back-hopping and correlation are counted as contributors to diffusion on the timescale accessible to our simulations, whereas these would not appear in a macroscopic measurement.

We have also mentioned the artificially high number of small rings due to periodic boundary conditions as a potential consequence of small supercell size. Table V suggests a possible correlation between smaller average ring size and a higher propensity to jump, particularly at the lower temperature, meaning our finite size effects

could result in a measurable increase in jump statistics and diffusion coefficients. However, any such decrease in average ring size from the periodic boundary conditions is likely to be accompanied by an increase in the overall number of rings. Since we have established the overall propensity for ring existence to inhibit hydrogen- and chemical-bond dynamics, the competition between these two effects should attenuate any potential impact on the macroscopic properties.

It should be noted that we are neglecting any quantum behavior of the protons. However, an analysis of experiments on CsDSO<sub>4</sub> suggests the isotope effect is relatively small<sup>28,29</sup>. In addition, theoretical work on the topologically similar material KDP<sup>30</sup> concluded that the predominant effect of quantum delocalization of the protons was limited to structural considerations, in that it decreased the H $\cdots$ O–H distance and consequently also the lattice parameter. The KDP analysis is also consistent with experimental comparisons of CsDSO<sub>4</sub> and CsHSO<sub>4</sub><sup>10,22</sup>.

A closer examination of the specific rate-limiting mechanisms covered in our analysis of proton diffusion in CsHSO<sub>4</sub> provides additional insight into the lack of any substantial isotope effect. Our findings indicate that the chemical-bond dynamics are much faster than previous analyses have suggested, of the same order as the hydrogen-bond dynamics. Rather, the primary limitation is manifest in the dynamics of the SO<sub>4</sub> tetrahedra, since these appear to govern the reversal rates of both chemical-bond jumping and hydrogen-bond hopping. Accounting for proton tunneling across the O–H $\cdots$ O double-well potential would therefore have little effect on the overall jump statistics, since the mobility of the SO<sub>4</sub> groups is classically controlled. In addition, we have established the importance of the chain and ring topology of the hydrogen-bond network in promoting diffusive events. However, changes in the topology are promoted by two factors—hydrogen-bond hopping and slow rotation of the SO<sub>4</sub> tetrahedra. Slow SO<sub>4</sub> rotation is clearly a classical phenomenon, and hydrogen-bond hopping is coupled to a 30° reorientation of the heavy SO<sub>4</sub> tetrahedron, meaning its dynamics are also ultimately classical.

## VIII. CONCLUSIONS

We have presented a detailed analysis of proton dynamics in superprotonic Phase-I CsHSO<sub>4</sub> based on first-principles molecular dynamics simulations. Our results confirm that the chemical-bond dynamics are dominated by local Grotthus-style hops which propagate successively along the hydrogen-bond network backbone. Individually, these hops are comparatively frequent, pointing to a low diffusion barrier, but the net effective rate of the chemical-bond dynamics is limited by an anomalously high rate of jump reversal. We find that the propensity for such forward- and back-hopping along the O–H $\cdots$ O complex is in turn heavily influenced by the dynamics of

TABLE V: Observed relative probabilities (%) for various hydrogen-bond network topologies in an ordinary timestep, compared with similar quantities for timesteps immediately preceding a chemical- or hydrogen-bond jump event. Also listed are the relevant average ring and chain sizes for frames where those topologies exist. Ring sizes are calculated based on the number of tetrahedra involved in the ring, whereas chain sizes denote the maximum individual branch length within the graph-theoretic tree structure. Data are from simulations at 550/620/750 K.

<i>Description</i>	<i>No jump</i>	<i>Hydrogen-bond jump</i>	<i>Chemical-bond jump</i>
Contains rings	71 / 78 / 52	64 / 72 / 49	47 / 55 / 28
Contains chains	60 / 74 / 70	69 / 81 / 75	83 / 87 / 84
Contains only rings	40 / 26 / 30	31 / 19 / 25	17 / 13 / 16
Contains only chains	29 / 22 / 48	36 / 28 / 51	53 / 45 / 72
Contains both rings and chains	31 / 52 / 22	34 / 52 / 24	29 / 42 / 12
Average ring size	5.6 / 4.5 / 4.7	5.3 / 4.5 / 4.6	4.9 / 4.5 / 4.5
Average chain size	6.9 / 5.4 / 6.2	6.9 / 5.4 / 6.0	6.8 / 5.6 / 6.0

the  $\text{SO}_4$  tetrahedra rather than by static local geometry alone.

We have also shown that the dynamics of the hydrogen-bond network are dominated by fast, discrete angular jumps between neighboring oxygens rather than by slow rotations of the  $\text{SO}_4$  tetrahedra. Such jumps occur with greater frequency between oxygens belonging to different  $\text{SO}_4$  tetrahedra than between oxygens of the same tetrahedron, by a factor of two or three. The hydrogen-bond jumps are accompanied by an approximately  $30^\circ$  reorientation of the participating  $\text{SO}_4$  tetrahedra to alleviate the lattice strain induced by the hop, thereby minimizing the likelihood of jump reversal. We have isolated a window of 50 fs for successful completion of this “fast” reorientation event and showed that it exists independently of a second, slower reorientation mechanism, operating on a timescale at least five times greater than its counterpart. The slower mechanism amounts to ordinary  $\text{SO}_4$  rotation on a longer timescale, and we propose this to be the dominant hydrogen-bond network reorientation mechanism for diffusion along the [001] direction, for which angular hops are significantly more difficult and less frequent, owing to the anisotropy of the  $\text{CsHSO}_4$  lattice.

Our topological analysis of the hydrogen-bond network revealed a significant number of branching and network-terminating nodes, indicating a substantial deviation from linearity, particularly at higher temperatures. We postulate that the underbound network terminators play a role in network reconfiguration by aiding  $\text{SO}_4$  rotational mobility. Graph-theoretic methodology offered a way to isolate chains and rings as dominant topological features in the network, and we discovered that the presence of chains and the absence of rings is a substantial predictor of likelihood for either a hydrogen- or chemical-bond jump event to occur. We propose that our topological analysis could be easily extended to similar well-defined, hydrogen-bonded network solids.

Finally, we apply our analysis to offer an explanation for the lack of a significant isotope effect in the  $\text{CsHSO}_4/\text{CsDSO}_4$  system. In particular, we tie both the chemical- and hydrogen-bond dynamics to the classical

dynamics of the  $\text{SO}_4$  tetrahedra and argue that the inclusion of proton quantum tunneling should play a relatively minor role in the rate-limiting steps of the diffusion mechanism.

## IX. ACKNOWLEDGMENTS

Funding for this work has been provided by the U.S. Department of Energy CSGF and MURI Grant DAAD 19-03-1-0169. Calculations have been done using the Quantum-ESPRESSO package<sup>21</sup> on computational facilities provided through NSF grant DMR-0414849.

## X. APPENDIX: GRAPH-THEORETIC METHODOLOGY

Here we offer a detailed account of the graph-theoretic methods used to calculate the hydrogen-bond network topology. We represent the network as a directed graph with the edge vector pointing along the  $\text{O-H}\cdots\text{O}$  bond direction; that is, from the sulfate tetrahedron acting as the hydrogen-bond donor in the complex to the sulfate tetrahedron acting as the hydrogen-bond acceptor. The adjacency matrix  $A_{ij}$  can then be constructed as an  $N \times N$  matrix, where  $N$  is the number of tetrahedra in the unit cell and the indices  $i$  and  $j$  run over the donor and acceptor sulfate groups, respectively:

$$A_{ij} = \begin{cases} 1 & \text{if there exists a direct link } i \rightarrow j \\ 0 & \text{otherwise} \end{cases}$$

The diagonal elements  $A_{ii}$  are set to zero. Topological characterization of a single node is then a straightforward process of performing a row sum to get the number of nodes to which it donates ( $N_d$ ) and a column sum to get the number of nodes donating to it ( $N_a$ ). It is also easy to categorize jump events by analyzing the difference of the adjacency matrices of successive timesteps.

To determine ring connectivity and size, we exploit the property of adjacency matrices<sup>31</sup> that element  $(i, j)$  of  $A^n$

gives the number of unique directed pathways from  $i$  to  $j$  of length  $n$ . We take the size of the ring containing the  $i^{\text{th}}$  node to be the lowest value of  $n$  in the interval  $[2, (N-1)]$  for which the diagonal element  $A_{ii}^n \neq 0$ . If  $A_{ii}^n = 0$  for all  $n$  in the interval, the node is not considered part of a ring.

Deriving chain sizes is somewhat more complex, since we must account for multiple branching topologies and for topological mixtures of rings and chains. We first decompose the network into clusters of unconnected subgraphs. This is done using the connectivity matrix  $C_{ij}$ , which has the property that  $C_{ij}=1$  if there is a path of *any length* connecting nodes  $i$  and  $j$ . We form the symmetric  $C_{ij}$  from  $A_{ij}$  using Warshall's algorithm<sup>32</sup>.

We proceed to construct a matrix  $S_{ij}$  that contains the shortest path between each pair of nodes  $(i, j)$ ,  $i \neq j$ , by taking the lowest value of  $n$  in the interval  $[2, (N-1)]$  for

which  $A_{ij}^n \neq 0$ . We can then take the maximum value of  $S_{ij}$  across the columns to get a row array of maximum path lengths for chains originating at the  $i^{\text{th}}$  node. The chain size is then determined by finding the maximum value of the resultant array over the nodes contained in each connected cluster, which can be easily determined by parsing  $C_{ij}$ . Finally, we add the restriction that none of the links in the chain can themselves be members of rings. This prevents counting of chains that are fictitiously long due to intermediate or terminating rings and ensures a clear separation between ring and chain topologies. The resulting chain size is then calculated as the maximum span of the graph-theoretic tree.

Very large networks may necessitate more efficient algorithms due to the expense of calculating  $A^{N-1}$ . However, the system sizes in our study are sufficiently small to readily allow calculations using the described method.

- 
- <sup>1</sup> A. I. Baranov, L. A. Shuvalov, and N. M. Shchagina, JETP Lett. **36**, 459 (1982).  
<sup>2</sup> S. M. Haile, D. A. Boysen, C. R. I. Chisholm, and R. B. Merle, Nature **410**, 910 (2001).  
<sup>3</sup> D. A. Boysen, T. Uda, C. R. I. Chisholm, and S. M. Haile, Science **303**, 68 (2004).  
<sup>4</sup> W. Münch, K. D. Kreuer, U. Traub, and J. Maier, Solid State Ion. **77**, 10 (1995).  
<sup>5</sup> W. Münch, K. D. Kreuer, U. Traub, and J. Maier, J. Mol. Struct. **281**, 1 (1996).  
<sup>6</sup> C. R. I. Chisholm, Y. H. Jang, S. M. Haile, and W. A. Goddard, Phys. Rev. B **72**, 134103 (2005).  
<sup>7</sup> X. Ke and I. Tanaka, Solid State Ion. **172**, 145 (2004).  
<sup>8</sup> X. Ke and I. Tanaka, Phys. Rev. B **69**, 165114 (2004).  
<sup>9</sup> M. Pham-Thi, P. Colomban, A. Novak, and R. Blinc, Solid State Commun. **55**, 265 (1985).  
<sup>10</sup> B. V. Merinov, A. I. Baranov, L. A. Shuvalov, and B. A. Maksimov, Kristallografiya **32**, 86 (1987).  
<sup>11</sup> K. D. Kreuer, Solid State Ion. **94**, 55 (1997).  
<sup>12</sup> A. V. Belushkin, R. L. McGreevy, P. Zetterstrom, and L. A. Shuvalov, Physica B **241-243**, 323 (1998).  
<sup>13</sup> P. Zetterström, A. V. Belushkin, R. L. McGreevy, and L. A. Shuvalov, Solid State Ion. **116**, 321 (1999).  
<sup>14</sup> J. C. Badot and P. Colomban, Solid State Ion. **35**, 143 (1989).  
<sup>15</sup> A. V. Belushkin, C. J. Carlile, and L. A. Shuvalov, J. Phys. Cond. Matt. **4**, 389 (1992).  
<sup>16</sup> R. Car and M. Parrinello, Phys. Rev. Lett. **55**, 2471 (1985).  
<sup>17</sup> S. Nosé, J. Chem. Phys. **81**, 511 (1984).  
<sup>18</sup> S. Nosé, Mol. Phys. **52**, 255 (1984).  
<sup>19</sup> W. G. Hoover, Phys. Rev. A **31**, 1695 (1985).  
<sup>20</sup> P. Perdew, K. Burke, and M. Ernzerhof, Phys. Rev. Lett. **77**, 3865 (1996).  
<sup>21</sup> S. Baroni, A. D. Corso, S. de Gironcoli, P. Giannozzi, C. Cavazzoni, G. Ballabio, S. Scandolo, G. Chiarotti, P. Focher, A. Pasquarello, et al., URL <http://www.quantum-espresso.org/>.  
<sup>22</sup> A. V. Belushkin, W. I. F. David, R. M. Ibberson, and L. A. Shuvalov, Acta Crystallogr. Sect. B **B47**, 161 (1991).  
<sup>23</sup> M. Mizuno and S. Hayashi, Solid State Ion. **167**, 317 (2004).  
<sup>24</sup> S. Hayashi and M. Mizuno, Solid State Commun. **132**, 443 (2004).  
<sup>25</sup> D. Laage and J. Hynes, Science **311**, 832 (2006).  
<sup>26</sup> Z. Jirak, M. Dlouha, S. Vratilav, A. M. Balagurov, A. I. Beskrovnyi, V. I. Gordelii, I. D. Datt, and L. A. Shuvalov, Phys. Status Solidi A **100**, K117 (1987).  
<sup>27</sup> A. V. Belushkin, C. J. Carlile, W. I. F. David, R. M. Ibberson, L. A. Shuvalov, and W. Zajac, Physica **174**, 268 (1991).  
<sup>28</sup> V. V. Sinitsyn, E. G. Ponyatovskii, A. I. Baranov, A. V. Tregubchenko, and L. Shuvalov, Sov. Phys. JETP **73**, 386 (1991).  
<sup>29</sup> K. D. Kreuer, Chem. Mat. **8**, 610 (1996).  
<sup>30</sup> S. Koval, J. Kohanoff, R. L. Migoni, and E. Tosatti, Phys. Rev. Lett. **89**, 187602 (2002).  
<sup>31</sup> C. D. Godsil and G. F. Royle, *Algebraic Graph Theory*, Graduate Texts in Mathematics (Springer-Verlag, 2001).  
<sup>32</sup> S. Warshall, J. Assoc. Comp. Machinery **9**, 11 (1962).